JPn Neuroscience
The Journal of Physiology

A method for detecting molecular transport within the cerebral ventricles of live zebrafish (*Danio rerio*) larvae

Maxwell H. Turner[1], Jeremy F.P. Ullmann[2] and Alan R. Kay[1]

[1] *Department of Biology, 336 BB, University of Iowa, Iowa City, IA 52242, USA*
[2] *Centre for Advanced Imaging, University of Queensland, St Lucia, Queensland 4072, Australia*

Key points

- The cerebral ventricles of the vertebrate brain form a series of interconnected chambers through which cerebrospinal fluid flows serving an important role in brain homeostasis and development.
- We introduce the larval zebrafish brain as a model for studying the physiology of the cerebral ventricles.
- The three dimensional form of the zebrafish ventricles was characterized by *in vivo* confocal microscopy and found to be similar to that of mammals.
- To follow the movement of molecules within ventricles we have a developed a technique using the uncaging of a fluorescent molecule.
- Zebrafish larvae provide a tractable model for studying ventricles and the movement of chemicals across the blood–brain barrier.

Abstract The production and flow of cerebrospinal fluid performs an important role in the development and homeostasis of the central nervous system. However, these processes are difficult to study in the mammalian brain because the ventricles are situated deep within the parenchyma. In this communication we introduce the zebrafish larva as an *in vivo* model for studying cerebral ventricle and blood–brain barrier function. Using confocal microscopy we show that zebrafish ventricles are topologically similar to those of the mammalian brain. We describe a new method for measuring the dynamics of molecular transport within the ventricles of live zebrafish by means of the uncaging of a fluorescein derivative. Furthermore, we determine that in 5–6 days post-fertilization zebrafish, the dispersal of molecules in the ventricles is driven by a combination of ciliary motion and diffusion. The zebrafish presents a tractable system with the advantage of genetics, size and transparency for exploring ventricular physiology and for mounting large-scale high throughput experiments.

(Resubmitted 7 December 2011; accepted after revision 22 February 2012; first published online 27 February 2012)
Corresponding author A. R. Kay: Department of Biology, University of Iowa, Iowa City, IA 52242, USA. Email: alan-kay@uiowa.edu
Present address for M.H. Turner: Graduate Program in Neurobiology and Behavior, University of Washington. Seattle, WA. 98195.

Abbreviations CA, cerebral aqueduct; CeP, cerebellar plate; CSF, cerebrospinal fluid; dpf, days post-fertilization; DV, diencephalic ventricle; E, epiphysis; hpf, hours post-fertilization; MO, medulla oblongata; P, pallium; RV, rhombencephalic ventricle; TeO, optic tectum; TeV, tectal ventricle; TV, telencephalic ventricle.

DOI: 10.1113/jphysiol.2011.225896

Introduction

Cerebral ventricles are a characteristic feature of all vertebrate brains (Jones, 1979) and are involved in a wide range of neurobiological functions, including mechanical cushioning of the brain, ionic homeostasis of the extracellular fluid (Davson *et al.* 1993) and neuronal migration and development (Sawamoto *et al.* 2006). The mature mammalian brain has four ventricles: two lateral ventricles, one in each hemisphere of the telencephalon; a third ventricle, located in the diencephalon; and a fourth ventricle, which lies in the hindbrain, adjacent to the cerebellum. The ventricles constitute a series of interconnected cavities within the vertebrate brain through which cerebrospinal fluid (CSF) flows. CSF is secreted by the choroid plexi, which are outfoldings of the ventricular walls, and flows out of the fourth ventricle into the subarachnoid space via the foramina of Luschka and Magendie. From the foramina the CSF flows around the external aspect of the brain within the subarachnoid space. The CSF completes its course through and around the brain by being reabsorbed into the venous circulation by the arachnoid granulations and villi.

There are a number of neurological disorders associated with malfunctions in the production and flow of CSF, such as hydrocephalus (Huh *et al.* 2009), while changes in ventricular volume have been reported in schizophrenia (Nopoulos *et al.* 1997) and autism (Hardan *et al.* 2001). In addition to functioning as a mechanical cushion for the brain, the CSF may be important in the homeostasis of the brain, serving as a conduit to clear potentially noxious substances like Aβ (Weller *et al.* 2009). There are also indications that ventricles and their associated outflow pathways may act as a passageway for immune cells in transit into and out of the brain (Thorne, 2004). Furthermore, the blood–brain barrier and the cerebral ventricles are of great importance in the distribution of therapeutic agents to the brain (Zlokovic, 2008; Pardridge, 2011).

Compared to other vertebrates, teleost fish have an unusual mechanism of brain development (Butler, 2000). In mammals the ventricular lumen is formed directly during the process of neurulation. However, in the teleost class of fish, the neural tube forms as a closed structure without a lumen, which then inflates 19 h after fertilization to form the ventricle. Expansion of the ventricles occurs prior to the formation of the choroid plexus requiring the activity of a Na^+,K^+-ATPase and cell shape changes but not cardiac activity (Lowery & Sive, 2009).

Here we introduce the zebrafish, *Danio rerio*, as a tractable model for studying cerebral ventricular physiology. In addition to a short generation time, transparent embryos, and relative ease of experimental manipulation, the zebrafish is a promising model for ventricular research because of the superficial location of the ventricles that facilitates their complete visualization (Lowery & Sive, 2009). To develop this model system, we have characterized the three-dimensional (3D) anatomy of the ventricles and introduced a method for measuring the transport of molecules in the CSF of live larval zebrafish by using a caged-fluorescein derivative (Ellis-Davies, 2007). This compound has a covalently attached group that quenches the fluorescence of the fluorophore and is cleaved off by exposure to UV light, effectively uncaging the fluorescein.

Methods

Ethical approval

Experiments were carried out in accordance with the NIH *Guide for the Care and Use of Laboratory Animals* and approved by the University of Iowa Institutional Animal Care and Use Committee as meeting the standards for humane animal care stipulated by the US Animal Welfare Act.

Sample preparation and fluorophore injections

Experiments were performed on 5- to 21-day-old zebrafish larvae, wild-type (WT) (AB strain) and *nacre* mutants, which have reduced pigmentation but only survive ∼4 weeks (Lister *et al.* 1999). 1-Phenyl-2-thiourea (PTU, Sigma P7629) at concentrations of 12–18 mg l^{-1} was used to inhibit melanogenesis (Karlsson *et al.* 2001). PTU treatment began before 24 h post-fertilization (hpf).

To prepare animals for injection and imaging sessions, approximately 0.5 ml of a solution containing low-gelling-point agarose (15 mg ml^{-1}, Sigma), 0.1 mg ml^{-1} MS-222 tricaine and 60 mg l^{-1} of aquarium sea salts at a temperature of ∼40°C was poured into a circular mould on a glass slide. Larvae were anaesthetized with tricaine (0.1–0.2 mg ml^{-1}) and transferred to the solidifying gel mixture. Larvae were positioned with the rostrocaudal axis of the head parallel to the surface of the slide and the dorsal surface of the head close to the surface of the agarose. The vitality of larvae was checked by monitoring the heartbeat and blood flow under bright field illumination.

Fluorophores were pressure injected into the RV using a glass micropipette with an approximate tip diameter of 10 μm and a Tritech Research microInjector. Approximately 2–6 nl of solution was injected at ∼15 psi with two 0.5–1.0 s pulses.

Animals were imaged on a Leica SP2 inverted confocal microscope or a Leica SPE upright confocal microscope. A 20× water-immersion objective could be used to resolve the small aqueducts connecting ventricular chambers, but

typically a 10× dry objective was sufficient to resolve the entire structure.

Fluorophores were prepared in a saline solution with the following composition (in mM): 140 NaCl, 2.5 KCl, 10 Hepes, 2 $CaCl_2$, at pH 7.4. FD-40, a 40,000 MW dextran-conjugated fluorescein (fluorescein isothiocyanate-dextran, FD40S Sigma) was used to image the anatomy of the ventricles. FD-40 was prepared at concentrations of ∼0.005% w/v in Hepes saline.

Tracking transport in the ventricles

For the uncaging experiments, a saline solution containing 0.5 mM CMNB-caged fluorescein (F7103 Invitrogen) and 2.1 mg ml^{-1} of 10,000 MW Texas Red-dextran was injected into the ventricle. First, the success of the injection was confirmed using excitation of the Texas Red with a 532 nm laser line. Next, to uncage fluorescein a 405 nm laser, at near-maximum intensity, was shone on a small (5–30 μm diameter) region of interest for 2–5 s, after a brief time series (15–30 s) of pre-uncaging fluorescence detection to establish a baseline, as exposure to ambient light during sample preparation uncages a small proportion of photo-activatable fluorescein. After the uncaging event, there was up to 7 min to detect the uncaged fluorescein. Scanning speed was favoured over spatial resolution, and each scanned image took 1.264 s.

ImageJ (NIH) was used to analyse photoactivation data and determine fluid flow patterns and transport rates. To quantify flow from these image series, the fluorescence intensities of a set of regions of interest (ROIs) along the rostrocaudal axis and running through the uncaging region were measured over time. Data were imported into OriginPro 7.0 (OriginLab Corp, Northampton, MA, USA) data analysis software, which was used to find the time at which peak fluorescence was reached in each successive region.

Estimating the diffusion coefficient

The concentration of a molecule at a distance r from the point at which it is deposited is given by (Crank, 1975):

$$c(r, t) = \frac{M}{(4\pi Dt)^{n/2}} \exp(-r^2/4Dt) \qquad (1)$$

where M is the initial amount of dye deposited, D the diffusion coefficient and n the dimensionality of the space (1, 2 or 3).

The time at which the concentration peaks as a given distance, r, can be found by taking the derivative of eqn (1) with respect to time and setting it equal to zero, giving the transport rate:

$$T^*(r) = \frac{2nD}{r} \qquad (2)$$

3D reconstruction

3D reconstructions were created using Amira 5.2.2 software (Visage Imaging, Inc., Richmond, Vic, Australia). Confocal image stacks were imported into Amira where Labelfield files were created with the same dimensions (voxel size and resolution) as the image stacks. Subsequently, the Segmentation Editor and the SurfaceGen module were used to label the ventricular system and create 3D reconstructions.

Results

Zebrafish ventricular anatomy

The 3D form of zebrafish ventricles was characterized by confocal microscopy after FD-40 was injected into the hindbrain ventricle. Full 3D reconstructions were performed in live wild-type (WT) zebrafish 5–7 days post-fertilization (dpf) (Fig. 1). Several 3D confocal scans were also performed on 21 dpf *nacre* mutants (Lister *et al.* 1999), which have reduced melanophore production and thus remain transparent for longer than WT animals (Fig. 2*A*), and these data confirm that the mature ventricle topology is present by 5–7 dpf.

The zebrafish cerebral ventricles include conspicuous chambers that are homologous to the four found in mammalian ventricles, though there exist several important differences (Fig. 1). In zebrafish, the central canal (not shown) of the spinal cord runs into the large hindbrain, rhombencephalic ventricle (RV), which has portions of its dorsal roof covered only by a thin epithelial layer. Rostral to the hindbrain ventricle is the cerebral aqueduct (CA), which runs ventral to the cerebellum and joins the diencephalic ventricle (DV) between the two optic tecta. The diencephalic ventricle continues rostrally to the telencephalic ventricle (TV). The zebrafish telencephalic ventricle lies between the two halves of the telencephalon and remains a single structure rather than two distinct lateral chambers, as is the case in mammals.

In addition to these three distinct ventricles and cerebral aqueduct, there are two lateral projections from the anterior CA which wrap around the caudal boundaries of each optic tectum; we therefore propose the names left and right tectal ventricles (TeV) for these cavities (Fig. 1).

Three-dimensional images constructed from confocal z-stacks exhibited clear ventral boundaries to all ventricular chambers. We also used two-photon imaging, which penetrates tissue more effectively than one-photon confocal, yet no extensions or new chamber was evident, confirming that our scans capture the full extent of the ventricles.

To determine the brain regions surrounding the ventricles we imaged H2A-GFP transgenic zebrafish (Pauls *et al.* 2001) expressing green fluorescent protein (GFP)

fused to the histone protein H2A in nuclei (Fig. 2*B*). In the 5–7 dpf zebrafish ventricles that we imaged in detail, we found no evidence for a subarachnoid space connected to the cerebral ventricular system ($n = 24$). Indeed, at points the ventricles appeared to be directly apposed to the skull (Fig. 2*C* and *D*).

To determine if dye injection inflated the ventricles we compared the depth of the RV in injected and un-injected

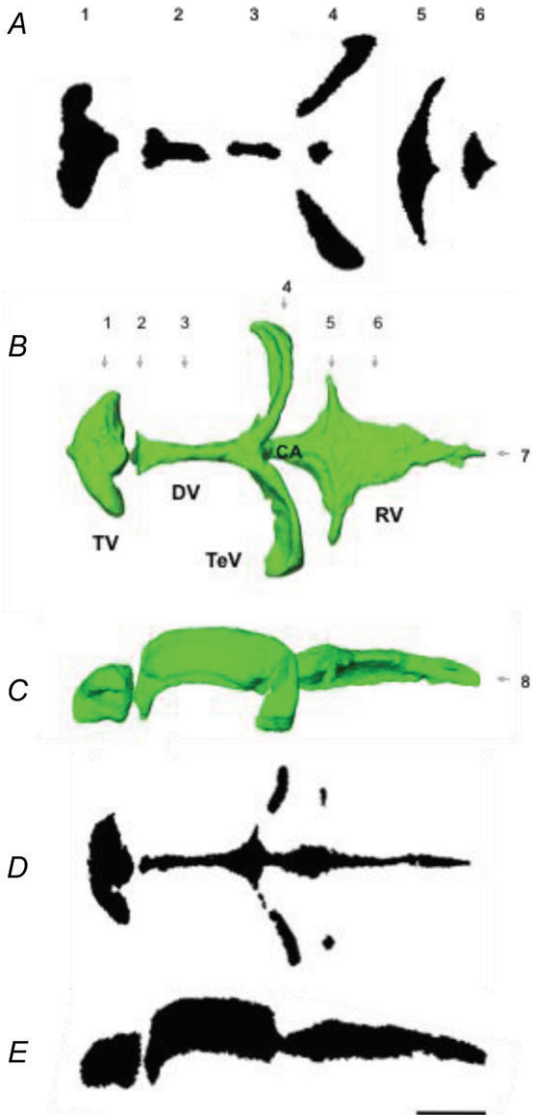

Figure 1. Three-dimensional renderings of a 6 dpf WT zebrafish's ventricles
3D renderings of the ventricular system are shown in panels *B* (dorsal view) and *C* (lateral view), while sections through the ventricles are shown in panels *A*, *D* and *E*. *A*, transverse sections through the ventricles with the level of the sections indicated by arrows 1–6 on *B*. Dorsal lies to the left. *D*, horizontal section at arrow 8 in *C*. *E*, sagittal section at arrow 7 in *B*. Scale bar is 100 μm and applies to all images. CA, cerebral aqueduct; DV, diencephalic ventricle; RV, rhombencephalic ventricle; TeV, tectal ventricle; TV, telencephalic ventricle.

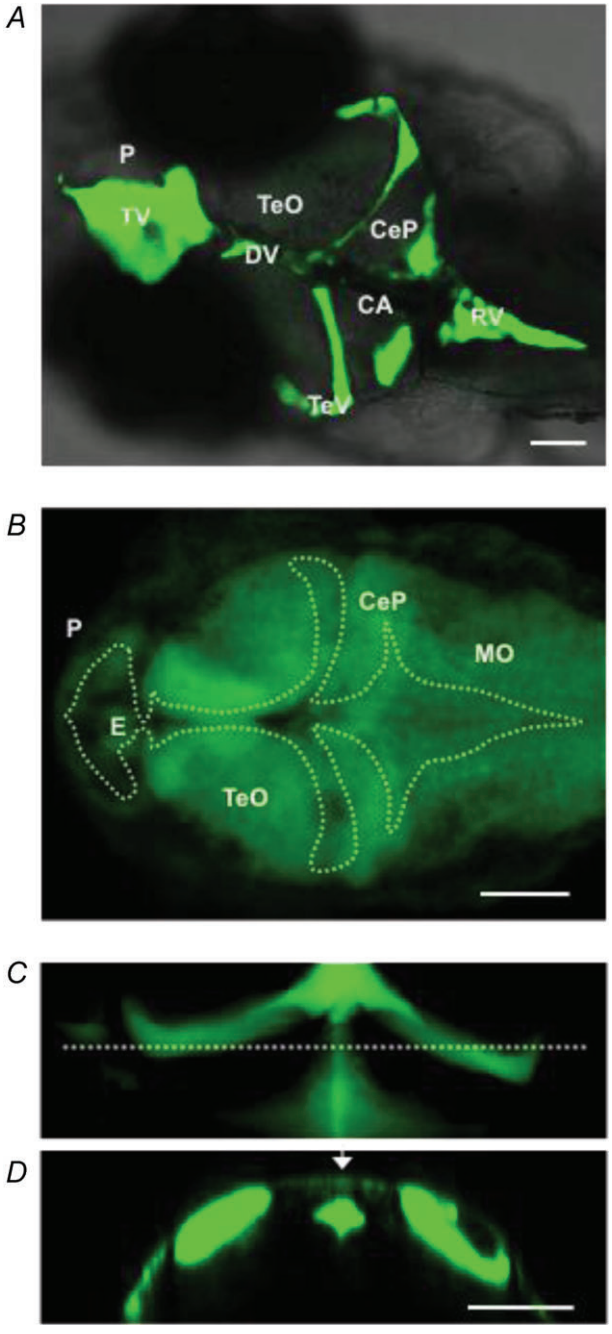

Figure 2. Structural views of zebrafish ventricular system
A, Z-projection of 21 dpf *nacre* mutant ventricular system. Rostral lies to the left. *B*, 5 dpf H2A-GFP transgenic zebrafish brain with outline of the ventricles superimposed. Regions of the brain were identified from Mueller & Wullimann (2005). Rostral lies to the left. *C*, dorsal view of 6 dpf WT zebrafish ventricle region showing TeV, CA, and anterior RV. Rostral lies to the top. *D*, transverse section through the dashed line in *C* showing cross-sections through the CA, and TeV. The autofluorescence of the surface of the animal demonstrates the close apposition of these ventricles to the skull (arrow). Scale bars are 100 μm. CA, cerebral aqueduct; CeP, cerebellar plate; DV, diencephalic ventricle; E, epiphysis; MO, medulla oblongata; P, pallium; RV, rhombencephalic ventricle; TeO, optic tectum; TeV, tectal ventricle; TV, telencephalic ventricle.

fish. In the latter case we examined the RV under bright field illumination in live zebrafish that were mounted on their sides. The depth of the ventricle was measured as indicated in Fig. 3*A* and *B*. For 5 dpf animals the average depth of the ventricle in un-injected fish was $40.1 \pm 9.7\ \mu$m (mean ± SD) ($n = 9$) and in injected fish $42.4 \pm 8.3\ \mu$m ($n = 5$). For 6 dpf fish the average depth of the ventricles in uninjected animals was $40.0 \pm 8.4\ \mu$m ($n = 7$) and in injected fish $39.5 \pm 4.7\ \mu$m ($n = 7$). There was a close correspondence between the size of the ventricles as viewed in uninjected H2A-GFP fish and those in injected WT fish (Fig. 3*C*). These results confirm that little expansion of the ventricles occurs under the conditions that we employed in this study.

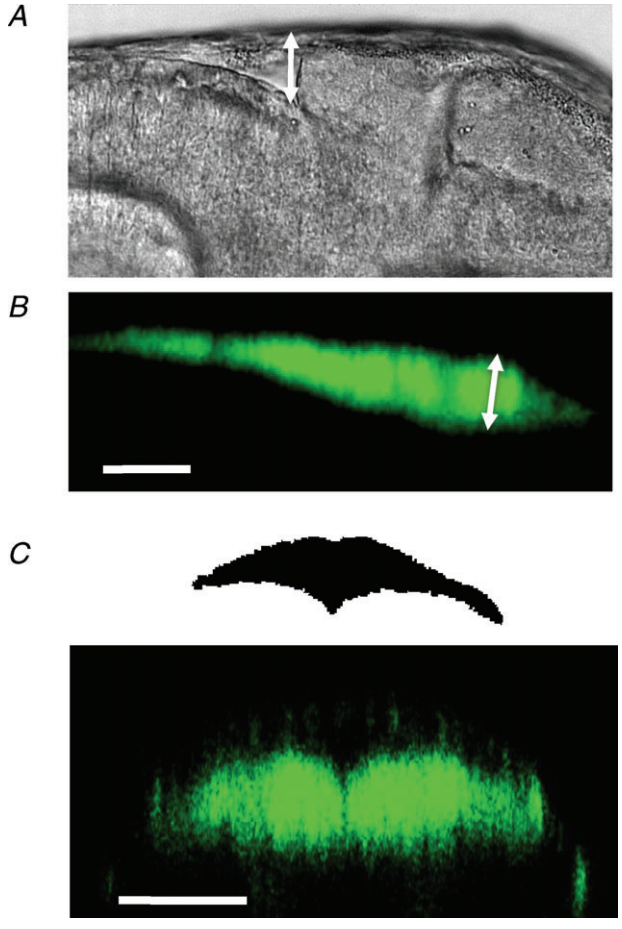

Figure 3. Ventricles are not inflated by dye injection
A, bright field image of live uninjected 5 dpf WT zebrafish showing the RV from the side. *B*, sagittal section of a live 5 dpf WT zebrafish injected with fluorescein-dextran. The RV depth was measured along a line orthogonal to the dorsal surface (double headed arrows). Scale bar 50 μm applies to panel *A* and *B*. *C*, transverse sections through a H2A-GFP fish (bottom) and WT fish injected with FD-40 (top, same as Fig. 1*A* (5)) at approximately the same level along the rostro–caudal axis. Scale bar 100 μm.

Transport in the ventricles

To detect movement in the CSF within zebrafish ventricles we initially used fluorescent beads (Ibanez-Tallon *et al.* 2004); however, the beads were rapidly trapped by cells within the ventricles (most likely microglia; Peri & Nusslein-Volhard, 2008), which prevented their free movement. A range of surface chemistries and charges were tested, but all were rapidly immobilized. We also examined fluorescence recovery after photobleaching (FRAP); however, it was difficult to follow the recovery. Finally, we employed a caged fluorescein (Ellis-Davies, 2007) derivative, which only fluoresces when unmasked by a pulse of light, to track CSF movement. The migration of the fluorescence through the ventricular system was then used to monitor molecular transport.

There are three potential mechanisms that can drive molecular movement within zebrafish ventricles: (a) production of CSF by the choroid plexus, (b) stirring of the CSF by ciliated ependymal cells, and (c) diffusion.

If the movement of molecules were driven by diffusion alone, a front of fluorescence should move roughly symmetrically from the centre of the site of uncaging ($x = 0$). Although it is not strictly correct to speak of the 'rate of diffusion' one can measure the time it takes for the fluorescence to peak at a given distance away from the centre of the laser flash and calculate a transport rate (T^*, see Methods). To model diffusion in the ventricles we used a quartz micro-cuvette with a rectangular cross-section and a depth of 50 μm (Fig. 4). Peak concentration was measured at a distance r from the site and exhibited a linear inverse dependence on r (see eqn (2)). Using this method, and assuming two-dimensional diffusion, $D = 481 \pm 41\ \mu\text{m}^2\ \text{s}^{-1}$ (mean ± SEM, $n = 4$), which accords well with prior estimates of the diffusion coefficient of fluorescein ($\sim 500\ \mu\text{m}^2\ \text{s}^{-1}$) (Fu *et al.* 1995).

To measure molecular transport within the zebrafish ventricles, caged fluorescein was injected into the RV, together with Texas red, which was used to determine the success of the injection. Confocal scans were acquired

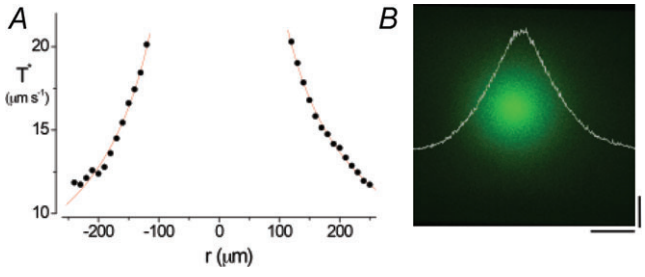

Figure 4. Temporal dynamics of an uncaging event in a rectangular microcuvette
A, T^* as a function of distance from the centre of the uncaging spot (line shows the fit to eqn (2)). *B*, image of the uncaged fluorescein a few seconds after the UV pulse. Scale bars, 100 μm and 10 au.

every 1.2 s after the uncaging pulse, with a delay of 5–9 s to the first measurement (Fig. 5*A*). To follow molecular transport the change in fluorescence intensity was measured as a function of time along a line through the site of photolysis along the rostro-caudal axis (Fig. 5*A*). There was some uptake of caged fluorescein by cells, which was visible as a static background against which the movement of free fluorophore occurred. To determine T^*, the fluorescence intensity was measured every 10 μm along the rostro-caudal axis. Examples of two experiments are shown in Fig. 5*B*, with the T^* plotted along the length of the rostro-caudal axis. The T^* profiles varied among animals; however they were all inconsistent with simple diffusion. Most profiles exhibited occasional increases in T^* with distance from the site of photolysis. None of the 18 ventricles characterized in detail exhibited the monotonic decline of T^* characteristic of diffusion (Fig. 4*A*). The increases in T^* and its non-monotonic course as a function of distance, are both borne out in the average T^* profile graphed in Fig. 5*C*.

Discussion

Ventricular system anatomy: a comparative analysis

The form of the zebrafish cerebral ventricles is similar to that of mammals. The cerebral aqueduct, rhombencephalic (mammalian fourth ventricle homologue), diencephalic (homologue of mammalian third ventricle), and telencephalic ventricles are all present in the zebrafish. In contrast to the mammalian forebrain ventricle, the zebrafish telencephalic ventricle is not divided into two lateral ventricles. It remains a medial structure with some lateral projection in the form of relatively thin regions superficial to the telencephalic halves. This is a consequence of the process of eversion during teleost telencephalic development (Butler, 2000). Another difference, and one of equal prominence, is the presence of two narrow lateral projections stemming from the anterior CA. The TeVs mark the boundary between the optic tecta and the cerebellum.

Transport in the zebrafish ventricles

Our uncaging experiments suggest that the transport of molecules within the CSF cannot be accounted for by diffusion or bulk flow. Instead, the dominant mechanism is likely to be the beating of cilia lining the ventricle walls. Cilia line the walls of mammalian ventricles, and have been found to direct CSF flow through the central canal of the spinal cord in the zebrafish (Kramer-Zucker, 2005). It is worth noting that the slowness of molecular movement *in vivo* (Fig. 5*C*) compared to that *in vitro* (Fig. 4*A*) suggests that the viscosity of CSF is higher than that of saline.

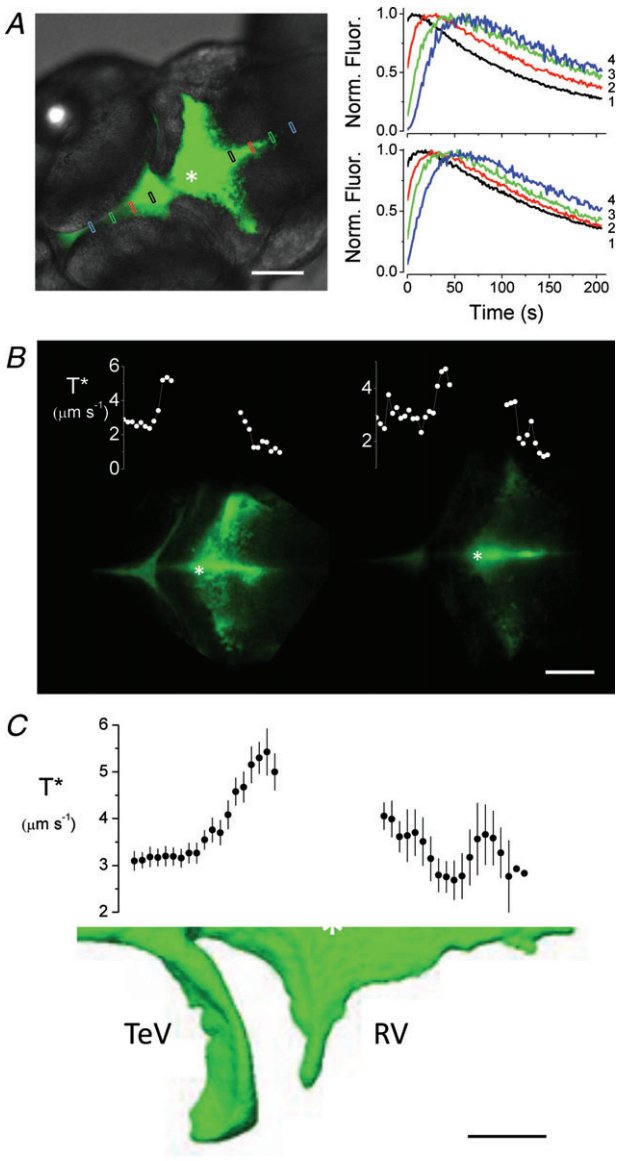

Figure 5. Tracking molecular transport within the zebrafish ventricles
A, representative data in CMNB-fluorescein uncaging experiments in a 5 dpf WT zebrafish. Left, a small region (*) at the anterior end of the RV is photolysed ($t = 0$) for approximately 2 s, after which uncaged fluorophore is tracked as it moves throughout the ventricles. Rostral lies to the bottom left. Right, normalized fluorescence as a function of time at the different areas of interest (1 closest to site of photolysis, 4 furthest). Top graph shows movement in the caudal direction and the bottom graph shows rostral transport. Scale bar is 50 μm. *B*, spread of fluorescence in 5 dpf WT zebrafish ventricles after photolysis at the position indicated by *. The transport rate (T^*) from two representative trials is plotted as a function of distance aligned with an image of the ventricles. Scale bar is 100 μm. *C*, average T^* as a function of distance from the site of photolysis (*), with a 3D rendering of the ventricles of a 6 dpf WT zebrafish (same as Fig. 1*B*) aligned with the graph (mean ± SEM, $n = 10$). Scale bar is 100 μm.

Recent work has shown that zebrafish choroid plexi, which produce CSF, develop in two regions of the dorsal ventricle walls: the first is the choroid plexus of the hindbrain, in the rhombencephalic ventricle; and the second in the telencephalic ventricle (García-Lecea *et al.* 2008). Unlike mammalian choroid plexi, the zebrafish's cannot be identified in low-power views and does not have the characteristic highly folded appearance. It is worth noting that the blood–brain barrier is established in zebrafish by 3 dpf (Xie *et al.* 2010)

We measured a total ventricular volume of 2.1 ± 0.92 nl (mean $\pm$ SD, $n = 5$). If we assume that the total volume of CSF is exchanged 4 times per day, comparable to the turnover rate measured in humans (Davson *et al.* 1993), and consider a simplified fluid flow model where CSF is secreted at one location, maintains laminar flow at a constant rate, and exits the system at another location, we can approximate the velocity of CSF flow under an advective fluid flow regime. The cerebral aqueduct is the narrowest ventricle segment, with a cross-sectional area of $709 \pm 237\ \mu m^2$ (mean $\pm$ SD). Estimates using this model give a CSF velocity through the cerebral aqueduct of $0.14\ \mu m\ s^{-1}$. As velocity is maximal at locations with minimum cross sectional area, this represents the highest CSF velocity under this model. Measured transport rates from photolysis experiments are much faster than the maximum velocity under the simplified advective model. Therefore, it seems likely that the flow in the larval zebrafish is dominated by beating of ependymal cilia, which have been described in teleosts (Cuoghi & Mola, 2009).

In recently published experiments (Miskevich, 2010) it was found that fluorescent beads injected into the ventricles of *Xenopus* tadpoles were driven largely by CSF production, since CSF flow declined when the heart stopped even though the cilia kept beating. Whether a particular animal exhibits flow dominated by CSF production or ciliary propulsion is likely to depend on the size of the ventricles. If the linear dimensions of a ventricle are increased by a factor x, for a constant exchange rate, the volume flow increases by a factor of x^3.

In the mammalian brain CSF produced within the ventricles largely by the choroid plexus flows into the subarachnoid space and then is taken up into the venous circulation by the arachnoid granulations (Davson *et al.* 1993; Pollay, 2010). From our studies in zebrafish it is unclear where the CSF flows once it leaves the confines of the ventricular system visible in our reconstructions. Whether the CSF flowing through the ventricles is transported into the extracellular space or is taken up by the venous system by specializations analogous to the arachnoid granulations remains to be seen (Jones, 1979).

Investigation of the mammalian ventricular system is made difficult by its location deep within the parenchyma, preventing the direct visualization of CSF. In contrast, the zebrafish ventricle provides a convenient model for studying CSF flow, allowing imaging of CSF production and flow in a live intact organism. Given the small size of the zebrafish, its short generation time, transparency and wealth of genetics, it should prove an excellent model system for exploring the passage of therapeutic agents across the blood brain–barrier (Neuwelt *et al.* 2011) particularly in automated high-content screening assays (Zanella *et al.* 2010).

References

Butler AB (2000). Topography and topology of the teleost telencephalon: a paradox resolved. *Neurosci Lett* **293**, 95–98.

Crank (1975). *The Mathematics of Diffusion*. Oxford University Press, Oxford.

Cuoghi B & Mola L (2009). Macroglial cells of the teleost central nervous system: a survey of the main types. *Cell Tissue Res* **338**, 319–332.

Davson H, Zlokovic B, Rakic L & Segal MB (1993). *An Introduction to the Blood-Brain Barrier*. CRC Press, Inc., Boca Raton, FL.

Ellis-Davies G (2007). Caged compounds: photorelease technology for control of cellular chemistry and physiology. *Nat Methods* **4**, 619–628.

Fu BM, Curry FE & Weinbaum S (1995). A diffusion wake model for tracer ultrastructure-permeability studies in microvessels. *Am J Physiol Heart Circ Physiol* **269**, H2124–2140.

García-Lecea M, Kondrychyn I, Fong S, Ye Z, Korzh V & Lopez-Schier H (2008). In vivo analysis of choroid plexus morphogenesis in zebrafish. *PLoS ONE* **3**, e3090.

Hardan AY, Minshew NJ, Mallikarjuhn M & Keshavan MS (2001). Brain volume in autism. *J Child Neurol* **16**, 421–424.

Huh MS, Todd MA & Picketts DJ (2009). SCO-ping out the mechanisms underlying the etiology of hydrocephalus. *Physiology (Bethesda)* **24**, 117–126.

Ibanez-Tallon I, Pagenstecher A, Fliegauf M, Olbrich H, Kispert A, Ketelsen UP, North A, Heintz N & Omran H (2004). Dysfunction of axonemal dynein heavy chain Mdnah5 inhibits ependymal flow and reveals a novel mechanism for hydrocephalus formation. *Hum Mol Genet* **13**, 2133–2141.

Jones HC (1979). Comparative aspects of the cerebrospinal fluid systems in vertebrates. *Sci Prog* **66**, 171–190.

Karlsson J, von Hofsten J & Olsson PE (2001). Generating transparent zebrafish: a refined method to improve detection of gene expression during embryonic development. *Mar Biotechnol (NY)* **3**, 522–527.

Kramer-Zucker A (2005). Cilia-driven fluid flow in the zebrafish pronephros, brain and Kupffer's vesicle is required for normal organogenesis. *Development* **132**, 1907–1921.

Lister JA, Robertson CP, Lepage T, Johnson SL & Raible DW (1999). *nacre* encodes a zebrafish microphthalmia-related protein that regulates neural-crest-derived pigment cell fate. *Development* **126**, 3757–3767.

Lowery LA & Sive H (2009). Totally tubular: the mystery behind function and origin of the brain ventricular system. *Bioessays* **31**, 446–458.
Miskevich F (2010). Imaging fluid flow and cilia beating pattern in *Xenopus* brain ventricles. *J Neurosci Methods* **189**, 1–4.
Mueller T & Wullimann MF (2005). *Atlas of Early Zebrafish Brain Development: A Tool for Molecular Neurogenetics*. Elsevier BV, Amsterdam.
Neuwelt EA, Bauer B, Fahlke C, Fricker G, Iadecola C, Janigro D, Leybaert L, Molnar Z, O'Donnell ME, Povlishock JT, Saunders NR, Sharp F, Stanimirovic D, Watts RJ & Drewes LR (2011). Engaging neuroscience to advance translational research in brain barrier biology. *Nat Rev Neurosci* **12**, 169–182.
Nopoulos P, Flaum M & Andreasen NC (1997). Sex differences in brain morphology in schizophrenia. *Am J Psychiatry* **154**, 1648–1654.
Pardridge WM (2011). Drug transport in brain via the cerebrospinal fluid. *Fluids Barriers CNS* **8**, 7.
Pauls S, Geldmacher-Voss B & Campos-Ortega JA (2001). A zebrafish histone variant H2A.F/Z and a transgenic H2A.F/Z:GFP fusion protein for in vivo studies of embryonic development. *Dev Genes Evol* **211**, 603–610.
Peri F & Nusslein-Volhard C (2008). Live imaging of neuronal degradation by microglia reveals a role for v0-ATPase a1 in phagosomal fusion in vivo. *Cell* **133**, 916–927.
Pollay M (2010). The function and structure of the cerebrospinal fluid outflow system. *Cerebrospinal Fluid Res* **7**, 9.
Sawamoto K, Wichterle H, Gonzalez-Perez O, Cholfin JA, Yamada M, Spassky N, Murcia NS, Garcia-Verdugo JM, Marin O, Rubenstein JL, Tessier-Lavigne M, Okano H & Alvarez-Buylla A (2006). New neurons follow the flow of cerebrospinal fluid in the adult brain. *Science* **311**, 629–632.
Thorne R (2004). Delivery of insulin-like growth factor-I to the rat brain and spinal cord along olfactory and trigeminal pathways following intranasal administration. *Neuroscience* **127**, 481–496.
Weller RO, Djuanda E, Yow HY & Carare RO (2009). Lymphatic drainage of the brain and the pathophysiology of neurological disease. *Acta Neuropathol* **117**, 1–14.
Xie J, Farage E, Sugimoto M & Anand-Apte B (2010). A novel transgenic zebrafish model for blood-brain and blood-retinal barrier development. *BMC Dev Biol* **10**, 76.
Zanella F, Lorens JB & Link W (2010). High content screening: seeing is believing. *Trends Biotechnol* **28**, 237–245.
Zlokovic B (2008). The blood-brain barrier in health and chronic neurodegenerative disorders. *Neuron* **57**, 178–201.

Author contributions

M.H.T. and A.R.K. conceived and designed the experiments. M.H.T. performed the experiments. M.H.T., J.F.P.U. and A.R.K. analysed the data. J.F.P.U. performed the 3D reconstructions. M.H.T. and A.R.K. drafted the manuscript with input from J.P.F.U. All authors approved the final version for publication.

Acknowledgements

We are very grateful to Dr Hazel Jones for helpful suggestions on an earlier version of this manuscript, Dr Bryan Bertoglio for kindling our interest in the cerebral ventricles and Drs Lisa Baye, Robert Cornell and Diane Slusarski for help and advice on raising zebrafish. The work was supported by a grant from NINDS (to A.R.K.), NIEHS through the University of Iowa Environmental Health Sciences Research centre, Grant NIEHS/NIH P30 ES056 (to A.R.K.).